Koci, Jack, Sidle, Roy C., Jarihani, Ben, and Cashman, Matthew J. (2020) ***Linking hydrological connectivity to gully erosion in savanna rangelands tributary to the Great Barrier Reef using structure-from-motion photogrammetry.*** **Land Degradation and Development, 31 (1) pp. 20-36.**

https://doi.org/10.1002/ldr.3421

Linking hydrological connectivity to gully erosion in savanna rangelands tributary to the Great Barrier Reef using Structure-from-Motion photogrammetry

Jack Koci[1*], Roy C. Sidle[1,2], Ben Jarihani[1], Matthew J. Cashman[3]

[1]Sustainability Research Centre, University of the Sunshine Coast, Maroochydore DC, Queensland 4558, Australia

[2]Mountain Societies Research Institute, University of Central Asia, Khorog GBAO 736000, Tajikistan

[3]US Geological Survey, MD/DE/DC Water Science Center, Baltimore, Maryland 21228, United States

***Corresponding author:** jack.koci@research.usc.edu.au

Running title: Hydrological connectivity and gully erosion in savanna rangelands

Acknowledgements

We are grateful to the landholders who hosted this research on their properties: Rob and Sue Bennetto; Margaret Calvert and Bill Norton; and John Ramsay and family. We are also grateful to the Commonwealth Scientific and Industrial Research Organisation (CSIRO), particularly Christian Roth, Rebecca Bartley, Scott Wilkinson and Aaron Hawdon, for facilitating access to the field sites, providing rainfall data presented in Supplementary Table 1, and for valuable discussion during the study. Anne Henderson (CSIRO) aided in the preparation of Figure 1. JK was supported by an Australian Government Research Training Program Scholarship; a CSIRO Post-graduate Scholarship; and a Meat and Livestock Australia Post-graduate Scholarship.

Koci J, Sidle RC, Jarihani B and Cashman MJ. (2020). Linking hydrological connectivity to gully erosion in savanna rangelands tributary to the Great Barrier Reef using Structure-from-Motion photogrammetry. Land Degradation and Development 31: 20-36. https://doi.org/10.1002/ldr.3421

ABSTRACT

Gully erosion is a major land management challenge globally and a particularly significant issue in dry-tropical savanna rangelands tributary to the Great Barrier Reef, Australia. This study investigated linkages between hillslope hydrological connectivity pathways and gully geomorphic change in the Burdekin River basin. High resolution (0.1 m) topographic and land cover data derived from low-cost aerial (via Unmanned Aircraft System, UAS) structure-from-motion with multi-view stereo photogrammetry (SfM) was used to map fine-scale connectivity patterns and quantify headcut retreat at the hillslope scale (~150,000 m^2). Very high resolution (0.01 m) topographic models derived from ground-based (via hand-held digital camera, GB) SfM, were used to quantify the morphology and geomorphic change of several gully arms (300-700 m^2) between 2016 and 2018. Median linear, areal, and volumetric headcut (n=21) retreat rates were 0.2 m yr^{-1}, 0.8 m^2 yr^{-1}, and 0.3 m^3 yr^{-1}, respectively. At all study sites, the points where modelled hydrological flow lines intersected gullies corresponded to observed geomorphic change, enabling spatially explicit identification of gully extension pathways as a result of overland flow. Application of an index of connectivity demarcated parts of the hillslope most connected to the gully network. Bare areas, roads and cattle trails were identified as important runoff source areas and hydrological conduits driving gully extension. GB SfM accurately reconstructed complex morphologic features including undercuts, overhangs, rills and flutes, providing insights into within-channel erosion processes. This study contributes to an improved understanding and modelling of hydrogeomorphic drivers of gully erosion in degraded savanna rangelands, ultimately benefiting gully management.

Keywords: Drone - hydrogeomorphology - index of connectivity - overland flow - runoff - Unmanned Aircraft System (UAS)

1 | INTRODUCTION

Gully erosion is a globally significant land degradation problem that reduces water quality (Bartley *et al.*, 2014a; Wantzen, 2006), decreases agricultural and rangeland productivity (Daba *et al.*, 2003; García-Ruiz, 2010), and damages infrastructure (Fox *et al.*, 2016; Jungerius *et al.*, 2002; Nyssen *et al.*, 2002). The hydrogeomorphic factors (e.g., rainfall, soil, topography, ground cover) and processes (e.g., seepage, piping, fluting, tension cracking and mass movement) driving gully development are complex, varying not only across spatial and temporal scales but also in specific form and process as gullies develop (Poesen *et al.*, 2003; Sidle *et al.*, 2019). While considerable progress has been made in our knowledge and understanding of these factors and processes during the past century (see recent reviews by Bocco, 2016; Castillo & Gómez, 2016; Poesen, 2018; Sidle *et al.*, 2019; Vanmaercke *et al.*, 2016), continued research is needed to improve our ability to accurately predict and model gully initiation, extension and stabilisation processes, erosion rates, and contributions to end-of-catchment sediment loads, as well as to inform optimal land management strategies (Poesen, 2018). Such research is particularly needed in tropical landscapes, which have received less attention than more temperate environments (Castillo & Gómez, 2016), despite widespread gully erosion in tropical settings (Sidle *et al.*, 2006; Thomas, 1994).

Recent advances in remote sensing techniques (e.g., Light Detection and Ranging, 'LiDAR', and Structure from Motion with Multi-View Stereo photogrammetry, 'SfM') and platforms (e.g., Unmanned Aircraft Systems, 'UAS'), have greatly improved our ability to understand and model the hydrogeomorphic factors and processes driving gully erosion (Sidle *et al.*, 2019). In recent years, SfM has become a major source of topographic data in the geosciences (Westoby *et al.*, 2012). This survey technique utilises multiple overlapping photographic images of a scene, taken from multiple viewpoints, to reconstruct three-dimensional (3D) landscape geometry (Smith *et al.*, 2015), providing a low-cost alternative to LiDAR. Images can be captured from both aerial (e.g., via UAS) and ground-based ('GB', e.g., via handheld digital camera) platforms (e.g., Callow *et al.*, 2018; Koci *et al.*, 2017). To date, most SfM research has focused on testing and refining the method and quantifying landscape geomorphic features (e.g., James *et al.*, 2017; Smith & Vericat, 2015). In gullied environments, SfM has been used to quantify the spatial distribution of gully systems as well as gully morphology (e.g. Castillo *et al.*, 2014; Frankl *et al.*, 2015; Glendell *et al.*, 2017; Kaiser *et al.*, 2014). Few studies have utilised both aerial and GB SfM data to quantify and describe gully erosion processes. Aerial SfM surveys can provide the spatial coverage necessary to capture important catchment characteristics (e.g., topography, land cover), but struggle to reconstruct complex morphologic surfaces (e.g., undercuts, overhangs), particularly when view of the ground is obscured by vegetation (Koci *et al.*, 2017). In contrast, GB SfM is more capable of quantifying fine-scale gully morphologic features, but is limited in survey extent. Thus, utilising aerial and GB SfM survey information offers great potential to better understand and model gully morphology, morphologic change, and the catchment characteristics driving gully development at different scales.

Topography is a particularly important hydrogeomorphic factor influencing gully erosion as it to a large extent dictates where runoff concentrates in the landscape (Patton & Schumm, 1975). In the past, topographic thresholds for gully head development have been widely employed based on empirical relationships between drainage area and slope (summarised in Torri & Poesen, 2014). A limitation of this approach is that it cannot provide spatially explicit information about gully extension pathways, or the key landscape factors that may be influencing gully evolution. The increasing accessibility of high resolution (sub-centimetre to sub-metre) topographic and land cover information derived from LiDAR and SfM (DeLong *et al.*, 2018; Liu, 2008; Smith *et al.*, 2015) is opening the door to more spatially explicit mapping and modelling of fine scale overland flow pathways (Heckmann & Vericat, 2018) and how these are linked to, and influence extension of, actively eroding systems.

The concept of hydrological and sediment 'connectivity' provides a useful framework for investigating the linkage between overland flow pathways and gully evolution. In general terms, hydrological and sediment connectivity describes the coupling of landforms (e.g., hillslopes to channels) and the associated linkages and transfers of water and sediment (Bracken & Croke, 2007; Heckmann *et al.*, 2018; Sidle *et al.*, 2017). Over the past 20 years, several connectivity indices have been described, such as the 'Volume to Breakthrough' approach of Bracken and Croke (2007) and the 'Network Index' of Lane *et al.* (2009). More recently, the topographically-based index of sediment connectivity (IC), originally proposed by Borselli *et al.* (2008) and later modified by Cavalli *et al.* (2013), has been developed to utilise high-resolution digital terrain models. The IC is strongly controlled by topography and considers the characteristics of the drainage area and the flow path length that a particle travels to arrive at the target (e.g., a channel or the catchment outlet). While the revised IC was developed in the context of mountainous alpine environments, it could potentially be used to characterise fine-scale spatial connectivity patterns in lower-gradient gullied catchments and thus determine where in the landscape runoff is likely to accumulate and therefore where gullies are likely to initiate and extend. Linking spatial connectivity maps with high resolution land cover information could also shed light into the influence of other landscape factors on gully development, such as the spatial distribution of vegetation (Bartley *et al.*, 2006; Ludwig *et al.*, 2005), as well as the presence of roads and trails (Croke *et al.*, 2005; Sidle *et al.*, 2004).

Gully erosion is a particularly significant issue in dry-tropical savanna rangelands tributary to the Great Barrier Reef (GBR) World Heritage Area, northeast Queensland, Australia (Bartley *et al.*, 2014a). In this region, the introduction of livestock grazing post-European settlement in the mid-1800s is suggested to have triggered widespread gully development (Bartley *et al.*, 2018; Hughes *et al.*, 2009; Lewis *et al.*, 2007; Shellberg *et al.*, 2010). Based on available mapping and modelling, there is an estimated 87,000 km of gullies in the GBR catchments (Wilkinson *et al.*, 2015). While early modelling studies originally suggested surface erosion (e.g., sheetwash, rilling) sources supplied most of the sediment to rivers in the region (e.g., McKergow *et al.*, 2005), recent sediment tracing studies (e.g., Caitcheon *et al.*, 2012; Olley *et al.*, 2013; Wilkinson *et al.*, 2013) and improved modelling estimates (e.g., McCloskey, 2017) now suggest that gully and bank erosion are the dominant sediment sources. The off-farm loss of sediments and particulate nutrients reduce productivity of grazing enterprises (Ash *et al.*, 2011; MacLeod & McIvor, 2008; Roth, 2004) and negatively impact downstream GBR ecosystems (Coles *et al.*, 2015; De'ath & Fabricius, 2010; Waterhouse *et al.*, 2017). Growing concerns about the declining health of the GBR's ecosystems have prompted large Government investments in gully remediation activities, in an effort to improve the quality of water entering the GBR (State of Queensland, 2018). However, it is widely acknowledged that effective gully erosion management in this region requires an improved understanding of the hydrogeomorphic factors and processes driving gully development (Shellberg *et al.*, 2013; Wilkinson *et al.*, 2018).

This study aims to investigate the linkages between hillslope hydrological connectivity and gully geomorphic change in savanna rangelands tributary to the GBR, using low-cost UAS and GB SfM. The study sites are located in the Burdekin River basin, which provides the largest source of sediment and particulate nutrients to the GBR (Bainbridge *et al.*, 2014; McCloskey, 2017). We first evaluate the accuracy of UAS and GB SfM topographic models of four hillslope gully systems within the Upper Burdekin catchment. We then quantify fine-scale hydrological flow pathways and link these to spatial patterns of gully geomorphic change over two wet seasons. Finally, we characterise hillslope hydrological connectivity patterns and investigate the influence of various landscape factors on flow routing. Our findings will contribute to an improved understanding and modelling of the hydrogeomorphic factors and processes involved in gully development in savanna landscapes, ultimately benefiting the management of gullies in tropical rangelands and elsewhere.

2 | MATERIALS AND METHODS

2.1 | Study site

The study sites are located in the Weany Creek (13.6 km^2) and Wheel Creek (10.5 km^2) sub-catchments within the Upper Burdekin Catchment (~36,000 km^2), a tributary to the Burdekin River basin (130,000 km^2) that drains to the GBR in northeast Queensland, Australia (Figure 1). The catchments have granodiorite lithology and the predominant soil classification is a Red Chromosol, a duplex sandy clay loam (Isbell, 1996). Chromosol soils cover approximately 12% of the Burdekin River basin and have been identified as erosion hotspots and therefore targets for management interventions (Gilad *et al.*, 2012). The climate is dry-tropical with two distinct seasons; a summer wet season between December and April and a dry season between May and November (Jarihani *et al.*, 2017). The mean annual rainfall (1900–2012) in the Weany and Wheel Creek catchments is 686 and 782 mm year^{-1}, respectively (Wilkinson *et al.*, 2018). Rainfall is subject to high interannual variability linked to the phase of the Southern Oscillation (Nicholls, 1991). Vegetation is characterised by a discontinuous upper stratum of *Eucalyptus* spp. and a more continuous understory of annual and perennial grasses, forbs, and small shrubs (Mott *et al.*, 1985). Cattle grazing commenced in the area after 1850 and remains the dominant land use today. Previous research (Bartley *et al.*, 2010; Bonell & Williams, 1987; McIvor *et al.*, 1995; Roth, 2004) and observations from our field studies indicate that infiltration excess or Hortonian overland flow (Horton, 1933) is a primary runoff generation process in this landscape, owing to the typically high rainfall intensities (Tables S1) and generally low soil infiltration capacity

(Figure S1). Saturation overland flow may also generate runoff during and following prolonged wet periods, most likely confined to saturated soils in riparian corridors, swales, and areas of shallow soil (Jarihani et al., 2017).

FIGURE 1

Across the Weany and Wheel Creek catchments, four hillslope gully systems were investigated, labelled ‘G1’, ‘G3’, ‘G6’ and ‘G8’. The gullies are classified as valley-side or valley-head gullies (Brice, 1966) and occur as linear or branching features along hillslope drainage lines. The selected sites are considered representative of the broader catchment, containing a diversity of gully features and ground cover conditions and have been the subject of previous studies (Koci *et al.*, 2017; Wilkinson *et al.*, 2018). UAS surveys covered the entire hillslope system (~150,000 m^2), while GB surveys covered a single gully within the broader system (~300–700 m^2). G1 is a V-shaped gully with two headcuts (1–1.5 m deep), steep sidewalls (45–90°), and a narrow gully floor (0.2–1 m wide) (Figure 2a). G3 is a U-shaped gully with a single distinct headcut (0.5 m deep) that sits below a small (~1 × 0.5 m deep) incised drainage depression, very steep sidewalls (70–90°) ranging in height from 1 to 2.5 m, and a slightly wider gully floor (1–1.5 m) (Figure 2b). G6 has a single main headcut (~1 m deep) that sits ~5 m downstream of two smaller headcuts (~0.3 m deep), sidewalls ranging in gradient from steep (45–90°) to more gentle (<45°), and gully bed widths ranging from 0.2 – 1 m (Figure 2c). G8 has multiple head cuts (0.5-1 m deep) in the upper 15 m and narrows into a more linear feature with V-shaped walls (45–90°) and a narrow gully floor (0.2–0.5 m wide) (Figure 2d).

FIGURE 2

2.2 | SfM workflow

UAS surveys of each hillslope gully system were completed in October 2017 and 2018 while GB surveys were completed in October 2016, 2017 and 2018 (Table 1) For each UAS survey, a DJI Phantom 4 Advanced quadcopter captured images at a height of 60 m in a double grid pattern with nadir viewing angle and 90% forward and 75% side overlap. To minimise the potential for vertical doming (James & Robson, 2014), a second set of images was captured in a double grid pattern with an off-nadir (30°) viewing angle, but with only 40% forward and side overlap. For the GB survey, images were captured with a hand-held Panasonic GH3 DSLR camera with a Panasonic Lumix G 20 mm (35 mm equivalent = 40 mm) prime lens, in a systematic pattern outlined in Koci et al. (2017). Ground control points (GCPs) were distributed across the survey areas and surveyed with a Real Time Kinematic Global Navigation Satellite System (RTK GNSS) receiver. Independent RTK

GNSS validation points were also collected at the time of each survey, covering the survey area of interest and individual gully cross-sections.

TABLE 1

Agisoft PhotoScan V1.4 (AgiSoft LLC, 2018) was used to process the UAS and GB imagery to produce georeferenced dense multi-view stereo point clouds and ortho-photo mosaics (Table 2). Mean georeferencing error was 0.03 m (min = 0.004, max = 0.08) for the GB survey and 0.07 m (min = 0.04, max = 0.09) for the UAS survey (Table S2). PhotoScan's point cloud classification procedure was used to remove trees and shrubs from the UAS dense point clouds, while preserving topographic detail in gullied areas.

TABLE 2

2.3 | DEM preparation and accuracy assessment

DEMs derived from the classified dense point clouds, were generated using the 'rasterize' tool in CloudCompare (v2.9) (Girardeau-Montaut, 2018). The minimum elevation point at each pixel was used to model the terrain surface, as it has the greatest chance to represent the surface within vegetated areas (Javernick *et al.*, 2014). The UAS-based DEMs (U-DEM) were generated at 0.1 m pixel size, whereas the Ground-based DEMs (G-DEM) were generated at 0.01 m pixel size. DEM elevation accuracy was evaluated outside of Agisoft PhotoScan by comparing elevation values of independently surveyed RTK GNSS points (i.e., RTK GNSS points not used in SfM georeferencing) with concordant points extracted from the DEM and presented as the root mean square error (RMSE). Additionally, survey repeatability was assessed by comparing DEMs produced from two GB surveys undertaken consecutively at each site, within each survey year, using the DEM of Difference (DoD) technique described in section 2.4.

2.4 | Geomorphic change

The assessment of geomorphic change between repeat U- and G-DEMs was conducted based on the DoD technique (Wheaton *et al.*, 2010), using the Geomorphic Change Detection v7.1 add-in (Riverscapes Consortium, 2018) to ArcGIS Desktop v10.6. A simple minimum level of detection (minLoD) was used to account for uncertainties in the DEMs (Brasington *et al.*, 2003) calculated as:

$$minLoD = t({\sigma_{Z1}}^2 + {\sigma_{Z2}}^2)^{0.5} \quad (1)$$

where, t is the critical t-value for a 95% confidence interval (t = 1.96), and σ_{Z1} and σ_{Z2} are estimated uncertainties of DEM_1 and DEM_2, respectively. DEM uncertainty was assumed to equal the RMSE of independently surveyed RTK GNSS validation points. To be consistent, the maximum minLOD for each survey technique was applied to all sites, equal to 0.3 m and 0.2 m, for the U- and G-DEMs, respectively.

2.5 | Flow pathways and the Index of Connectivity

Raw DEMs must be hydrologically corrected prior to hydrogeomorphic analyses (Jarihani *et al.*, 2015). In this study, U-DEMs were hydrologically corrected in WhiteBox Geospatial Analysis Tools v3.4 software package (Lindsay, 2016) using the Breach Depressions tool. This tool removes topographic depressions and apparent dams in the DEM in order to enforce continuous flow by breaching through topographic barriers. ArcGIS was then used to quantify flow direction (D-Infinity) and flow accumulation. Flow accumulation was reclassified to show only flow lines with a contributing area > 10 m^2 (minor flow lines) and > 100 m^2 (major flow lines).

The IC was computed in ArcGIS using the Connectivity Index ArcGIS toolbox (Cavalli, 2016), according to the equation:

$$IC = \log_{10}\left(\frac{D_{up}}{D_{dn}}\right) = \log_{10}\left(\frac{\overline{W}.\overline{S}.\sqrt{A}}{\sum_i \frac{d_i}{W_i.S_i}}\right) \qquad (2)$$

where D_{up} is the upslope component and refers to the potential for downstream routing of water and sediment produced upslope, D_{dn} is the downslope component and takes into account the flow path length that a particle travels to arrive at the nearest target or sink, $\overline{W}$ is the average weighting factor of the upslope contributing area (dimensionless), $\overline{S}$ is the average slope gradient of the upslope contributing area (m/m), A is the upslope contributing area (m^2), d_i is the length of the flow path along the i^{th} cell according to the steepest downslope direction (m), and W_i and S_i are the weighting factor and slope gradient of the i^{th} cell, respectively. The weighting factor (W) used to model the impedance to runoff and sediment movement is a local measure of topographic surface roughness, derived from high resolution DEMs. IC can assume values ranging from $-\infty$ to $+\infty$, with connectivity increasing for larger IC values. The 'IC Channel' function was used to show the potential connection of water and sediment between the hillslope and the perimeter of the gully of interest. The 'IC Outlet' function was used to show connectivity patterns within specific gully headcuts of interest. The IC was selected because it: (i) is a distributed geomorphometric index, easily derived from a DEM, (ii) can be computed with reference to specific target features (i.e., gullies), and (iii) has been adapted for high-resolution DEMs.

3 | RESULTS

3.1 | Structure-from-Motion DEM accuracy

Across the hillslope, RMSE in elevation of U-DEMs ranges from 0.06 to 0.12 m (Table 3). Across individual gullies, overall RMSE in elevation of G-DEMs, ranges from 0.03 to 0.08 m. The distribution of elevation error is approximately normal, although there is variation in skewness (Figure 3a, b). Visual analysis of the spatial distribution in elevation error (Figure 3c, d) shows that higher elevation errors are often in areas of dense ground cover or complex morphology (e.g., steep gully sides, undercuts). Both U- and G-DEMs provide good representations of gully cross-sectional profiles, closely mirroring the profiles surveyed by RTK GNSS (Figure 3e, f). Overall RMSE between DEMs produced from two separate GB surveys of the same site, collected consecutively, ranges from 0.02 to 0.09 m.

TABLE 3

3.2 | Hydrological flow pathways and gully geomorphic change

Geomorphic change (> the minLOD) occurred in all four gully arms between 2016 and 2018, with most erosion between 2017 and 2018 (Table 4), corresponding to increased annual rainfall (Table S1). At G1, the net erosion volume between 2016 and 2018 was 17.1 m^3, while headcut retreat was ~0.4 m. A major flow line (contributing area >100 m^2, Figure 4a left panel) intersects G1 at each headcut, corresponding to areas of greatest geomorphic change (Figure 4a right panel). Inspection of the 3D GB SfM model (Figure 2a) show significant scour and undercutting around the base of the headcuts. A convergence of minor flow lines (contributing area >10 m^2, Figure 4a right panel) on the upper left side of the gully, immediately downstream of where the two main headcuts converge, is driving the development of a new lateral headcut. Several other minor flow lines intersect the gully sides, contributing to localised rilling, fluting, and sheet wash. Scouring and deepening of the gully bed and lower sections of the side walls is evident. Weathered bedrock is exposed in some sections of the gully bed. At G3, the net erosion volume between 2016 and 2018 was 3.0 m^3, while headcut retreat was ~0.3 m. Erosion primarily occurs at the gully head, corresponding to the intersection of two major flow lines (Figure 4b). Weathered bedrock is exposed in the gully bed along the entire length of the gully. No major flow lines intersect the gully sides, resulting in a mostly linear morphology. At G6, the net erosion volume between 2016 and 2018 was 3.1 m^3, while headcut retreat was ~0.1 m. Unlike G1 and G3, two major flow lines, and several minor flow lines intersect the gully sides, which may contribute to gully widening (Figure 4c). The more gently sloping sides of G6, however, are vegetated with trees, grasses, and small shrubs, which may effectively stabilise the banks. Weathered bedrock is exposed at the main gully head, reducing the rate of headcut retreat. Two small headcuts have formed ~5 m upstream of the main headcut, corresponding to the intersection of two major flow lines. At G8, the net erosion volume between 2016 and 2018 was 18.5 m^3, while head cut retreat was ~0.1 – 0.7 m. Multiple major and minor flow lines intersect the upper half of the gully, resulting in channel bifurcation (Figure 4d). There is evidence of mass wasting, riling, and fluting at these headcuts and along the gully edges.

TABLE 4

FIGURE 4

3.3 | Hillslope hydrological connectivity

The hydrological connectivity maps (Figure 5) show the potential connection of water and sediment between the hillslope and the main gully system. As expected, across all hillslopes, connectivity is generally highest closest to the main channel and progressively decreases away from it. Across the hillslope however, lines of high IC values are clearly demarcated around major flow concentration areas, indicating the primary pathways which route water and sediment toward the gully. Being areas of high flow accumulation and low surface roughness, high IC pathways are good indicators of the most likely paths of gully extension. At G1 headcut 1 (G1HC1) (Figure 5a) for example, the existing headcut is likely to split in two, with one headcut extending to the north-west and the other to north-east. Examination of the 3D GB model supports this interpretation, with clear signs of headcut divergence (see inset in Figure 5a). Similarly, at G3HC1, the existing headcut is likely to split in two, with one headcut extending to the north and the other to north-east (Figure 5b).

Linking the location of high IC pathways with high resolution ortho-photo mosaics enables interpretation of the likely sources of runoff generation and flow routing. At G1HC1 (Figure 5a) for example, the high IC pathway extending north-east toward the catchment boundary aligns with a cattle trail, which captures a large proportion of runoff from the upper part of the catchment and routes it toward the gully head. At G3 (Figure 5b), a number of scalded (i.e., persistently bare) areas and cattle trails, as well as an old access road in the upper catchment are highly connected to the gully system. Similarly, at G6HC5 (Figure 5c), a ditch diverting water off of an unsealed road at the top of the catchment is linked directly to the gully head. At G8 (Figure 5d), ground cover is uniformly low, numerous cattle trails lead directly to the gully head, and an unsealed road at the top of the catchment is directly connected to the gully system (Figure 6). The cumulative effect of these catchment characteristics is that runoff is delivered efficiently to gullies, resulting in relatively high headcut retreat rates at G8 (Table 5).

FIGURE 5

FIGURE 6

Between 2017 and 2018, median linear, areal, and volumetric headcut (n=21) retreat rates were 0.2 m yr^{-1} (range: 0 – 0.3 m yr^{-1}), 0.8 m^{2} yr^{-1} (range: 0 – 9.0 m^{2} yr^{-1}), and 0.3 m^{3} yr^{-1} (range: 0 – 4.2 m^{3} yr^{-1}), respectively (Table 5). There is no relationship between volumetric headcut retreat and: (i) headcut catchment area; (ii) headcut mean catchment slope; or (ii) headcut mean IC value (Figure 7).

TABLE 5

FIGURE 7

4 | DISCUSSION

4.1 | Linking hillslope connectivity to gully erosion

High resolution (0.1 m) mapping of fine-scale hydrological flow pathways (derived from UAS SfM), coupled with very high resolution (0.01 m) topographic modelling of individual gully arms (derived from GB SfM), enables spatially explicit identification of where gully expansion is most likely to occur and provides insights into key within-channel erosion processes. At all study sites, the points at which modelled flow pathways intersected the main gully channel, corresponded to observed geomorphic change between 2016 and 2018 (Figure 4). Most of the extension occurred at the gully heads as a result of waterfall and plunge-pool erosion, scouring around the base of the headcut, undermining the back walls, and eventually leading to mass failure (Bull & Kirkby, 1997). Where flow pathways intersected the gully sides, rilling and fluting features were present, and in some cases were developing into new lateral headcuts (e.g., at G1 and G8). Scouring and deepening of the gully bed was also evident, although exposure of weathered bedrock at all sites suggest further deepening may be limited. While minimal gully wall erosion (and therefore widening) was observed during the relatively short study period, longer-term studies in the region suggest that gully wall erosion is also an important sediment source (Wilkinson *et al.*, 2018). Given the dispersive nature of Chromosol soils (Chittleborough, 1992), soil piping processes may also lead to bank instability in some areas (Fox & Wilson, 2010), but this was not observed. Further analysis of within-channel erosion processes and extension pathways would greatly benefit from the coupling of repeat high resolution topographic surveys as described in this study, with physical measurements (e.g., soil structural stability, hydraulic conductivity, gully discharge) in and around actively eroding gullies.

High resolution mapping of hillslope connectivity patterns, using the IC (Cavalli *et al.*, 2013), enables spatially explicit identification of the primary flow pathways routing water and sediment toward the gully (Figure 5). Being areas of high flow accumulation and low surface roughness, high IC pathways are good indicators of the most likely paths of gully extension and can help to identify the key landscape factors influencing gully evolution. In this study, overlaying IC maps with high resolution ortho-photo mosaics, revealed particularly high connectivity in areas of low ground cover, and direct linkages between actively eroding gullies and roads and cattle trails. Previous research has highlighted the critical role that bare patches play in generating runoff on savanna hillslopes (Bartley *et al.*, 2010; Ludwig *et al.*, 2005; Ryan *et al.*, 2015), but the effect of roads and cattle trails has received less attention (Croke *et al.*, 2005; Sidle *et al.*, 2004). Roads and trails have very low hydraulic conductivity (Figure S1), which not only generate Hortonian overland flow, but also intercept runoff from upslope and adjacent areas, which can be directed towards the gully system (Sidle & Ziegler, 2010; Sidle *et al.*, 2006). While further research is needed to quantify the degree to which roads and trails increase hydrological connectivity in these savanna rangelands, it is clear these features are important runoff source areas and hydrological conduits driving gully extension and should be given greater consideration in catchment management activities.

Along with more traditional metrics such as slope and area, calculating the IC with respect to major headcuts within each hillslope has potential to provide additional information about the relative susceptibility of an area to headcut retreat. Hillslopes with higher hydrological connectivity are expected to be more susceptible to runoff and erosion and therefore exhibit greater geomorphic change. In this study, however, a clear relationship between volumetric headcut retreat rates and mean IC values was not established (Figure 7). This is likely due to the limited geomorphic change observed over the one monitored wet season (Table 5), as well as differences in rainfall among the catchments which produce variable headcut retreat rates (Table S1).

The median rate of linear (0.2 m yr^{-1}), areal (0.8 m^2 yr^{-1}), and volumetric headcut retreat (0.3 m^3 yr^{-1}) between 2017 and 2018 (Table 5), are somewhat lower than estimated global median headcut retreat rates of 0.89 m yr^{-1}, 3.12 m^2 yr^{-1} and 2.2 m^3 yr^{-1}, respectively (Vanmaercke *et al.*, 2016), although are in line with those reported by other studies of hillslope gullies in the region (e.g., Wilkinson *et al.*, 2018). Other studies of typically larger 'alluvial' gullies, which are incised into and drain alluvial deposits, along high stream-order and main river channels, have reported higher retreat rates of <0.5 m yr^{-1} to >10 m yr^{-1} in some extreme cases (Brooks *et al.*, 2009; Shellberg *et al.*, 2016). It is worth noting, while annual rainfall during the study period was within ~20% of the long-term average, few large rainfall events (i.e., daily rainfall > 50 mm) were observed (Table S1). Large and intense rainfall events, such as those associated with monsoonal lows or tropical cyclones, have been shown to generate large runoff volumes, irrespective of vegetation cover (Bartley *et al.*, 2014b; McIvor *et al.*, 1995; Roth, 2004), and therefore have the potential to produce greater headcut retreat rates than those reported here. Longer-term monitoring (~5-15 years) of gully retreat rates is needed to account for the highly variable climatic conditions typical of these tropical landscapes (Bartley *et al.*, 2014b). Ideally, such monitoring should encompass the full spectrum of gully types and stages of evolution, and include measurement of local soil, vegetation, land use and rainfall characteristics, at different scales (Sidle *et al.*, 2017). This information would aid in the development of improved process-based models capable of predicting erosion rates and potential contributions to end-of-catchment sediment loads (Poesen, 2018; Sidle *et al.*, 2019).

This study applied a previously developed index of connectivity (Cavalli *et al.*, 2013) which primarily considers topographic controls on hydrological and sediment connectivity. Moving forward, future development and application of connectivity indices in this landscape should consider the incorporation of other important hydrogeomorphic parameters, such as vegetation, rainfall and soil characteristics. For example, in addition to topographic information, the spatial distribution and characteristics of vegetation cover could be extracted from SfM or LiDAR survey data and used as roughness parameters within the existing IC algorithm (e.g., Lizaga *et al.*, 2018). Where spatially distributed rainfall information is available, rainfall erosivity could be also incorporated into the IC (e.g., Chartin *et al.*, 2017), as could spatially distributed soil infiltration and erodibility (e.g., Gay *et al.*, 2016). A multi-parameter connectivity index could potentially provide a more robust representation of water and sediment transfer pathways across gullied savanna landscapes and would enable assessment of how connectivity changes in response to natural variations in vegetation and rainfall. Such assessments would benefit from an evaluation of the optimum resolution of topographic and landscape data required for different applications (e.g., Jarihani *et al.*, 2015). Preliminary analysis in this study suggests that DEM resolutions of 0.1-0.5 m would be suitable for quantification of fine-scale connectivity patterns at the hillslope scale (e.g., 1-25 ha), while lower resolution (e.g., 1-2 m) DEMs would be more suitable at the small catchment scale (e.g., 10 – 20 km^2), but this requires further validation. Finally, further development of connectivity indices should be supported by field studies aimed at validating predicted spatial patterns of connectivity as well establishing relationships between index values and actual water and sediment transfer and yields (Heckmann *et al.*, 2018).

4.2 | Using Structure-from-Motion photogrammetry in land management activities

This study demonstrates that low-cost aerial and ground-based SfM survey techniques can produce high resolution and accurate topographic and landcover data within gullied savanna rangelands at different scales, proving valuable information for land management. At the hillslope scale (~1-25 ha), low-altitude (e.g., ~ 60-100 m above ground level) aerial SfM can be used to rapidly inventory catchment characteristics that may be influencing gully evolution (e.g., topography, hydrological flow pathways, vegetation patterns, roads and trails). An IC can then be developed with this information and used to identify specific catchment areas and/or gully systems most connected to a specific point of interest (e.g., the catchment outlet), and therefore prioritised for management intervention. Once a priority area has been identified, more detailed mapping and monitoring can then be implemented. For example, in situations where detailed information about gully morphology (e.g., undercuts, overhangs) and fine-scale morphological change is required, GB SfM can be used to produce very high-resolution (0.01 m) topographic models of individual gully arms and erosion features (~0.001-0.1 ha). This information is often lost in aerial SfM surveys, particularly when view of these features is obscured by vegetation. Identification of intersection points between hydrological flow pathways and the actively eroding gully, together with knowledge of the main within-channel erosion processes, can then be used to guide decisions about the most effective erosion control measures (Kirkby & Bracken, 2009; Prosser & Winchester, 1996; Wilkinson *et al.*, 2018). For example, if mass failure at the gully head is the primary erosion mechanism, erosion control should aim to reduce overland flow concentration within the headcut catchment area, for example through revegetation and tree planting, reduced stocking density, and/or fencing. If gully walls are eroding, then revegetation along the side walls may help to stabilise the banks. If the gully floor is scouring, then porous check dams may reduce gully sediment yield. Once an intervention has been put in place, repeat SfM surveys over time (~5-15 years) would enable detailed analysis of landscape recovery related to the effectiveness of gully remediation measures.

It must be noted, while the SfM workflow is relatively straightforward to implement, practitioners should be aware of its limitations (Koci et al., 2017) and thoroughly consider different elements of survey design and processing (James *et al.*, 2017). Surveying densely vegetated areas, for example, remains particularly problematic and, in this study, forced the exclusion of two additional sites from the analysis. Despite a rapid uptake of SfM by the geosciences community (Smith et al., 2015), there remains some uncertainty as to optimal survey and processing designs in different landscapes and geomorphological applications, and so continued technical research is required. The approach documented in this study, for example, would benefit from further testing to determine the optimum number, overlap, height and angle of image of acquisition, as well as the optimum number and distribution of GCPs. Such testing would enable faster and more efficient surveys and processing and may help to further improve model accuracy.

5 | CONCLUSION

This study sought to investigate linkages between hillslope hydrological connectivity pathways and gully geomorphic change in savanna rangelands tributary to the GBR, using low-cost UAS and GB SfM. Both UAS and GB survey techniques delivered high resolution and accurate topographic models of gullied hillslopes. These topographic models were used to map fine-scale hydrological flow pathways and derive an index of hydrological connectivity, providing spatially explicit information about where gully extension is most likely to occur due to overland flow and insights into landscape factors contributing to gully extension (e.g., scalded or bare areas, roads, and cattle trails). Examination of very high-resolution 3D SfM models allowed interpretation of the dominant within-channel processes driving gully extension, including mass wasting, particularly at the gully head, rilling and fluting along the gully sides, and gully bed scour. As such, this study contributes to an improved understanding and modelling of gully erosion in savanna landscapes, ultimately benefiting the management of gullies in tropical rangelands and elsewhere.

REFERENCES

AgiSoft LLC. (2018). AgiSoft PhotoScan Professional V1.4 Accessed 3 July 2018. Retrieved from http://www.agisoft.com/downloads/user-manuals/

Ash, A. J., Corfield, J. P., McIvor, J. G., & Ksiksi, T. S. (2011). Grazing management in tropical savannas: Utilization and rest Strategies to manipulate rangeland condition. *Rangeland Ecology & Management, 64*, 223-239. doi:https://doi.org/10.2111/REM-D-09-00111.1

Bainbridge, Z. T., Lewis, S. E., Smithers, S. G., Kuhnert, P. M., Henderson, B. L., & Brodie, J. E. (2014). Fine suspended sediment and water budgets for a large, seasonally dry tropical catchment: Burdekin River catchment, Queensland, Australia. *Water Resources Research, 50*(11), 9067-9087. doi:https://doi.org/10.1002/2013WR014386

Bartley, R., Bainbridge, Z. T., Lewis, S. E., Kroon, F. J., Wilkinson, S. N., Brodie, J. E., & Silburn, D. M. (2014a). Relating sediment impacts on coral reefs to watershed sources, processes and management: A review. *Science of the Total Environment, 468–469*, 1138-1153. doi:https://doi.org/10.1016/j.scitotenv.2013.09.030

Bartley, R., Corfield, J. P., Abbott, B. N., Hawdon, A. A., Wilkinson, S. N., & Nelson, B. (2010). Impacts of improved grazing land management on sediment yields, Part 1: Hillslope processes. *Journal of hydrology, 389*, 237-248. doi:http://dx.doi.org/10.1016/j.jhydrol.2010.05.002

Bartley, R., Corfield, J. P., Hawdon, A. A., Kinsey-Henderson, A. E., Abbott, B. N., Wilkinson, S. N., & Keen, R. J. (2014b). Can changes to pasture management reduce runoff and sediment loss to the Great Barrier Reef? The results of a 10-year study in the Burdekin catchment, Australia. *The Rangeland Journal, 36*(1), 67-84. doi:http://dx.doi.org/10.1071/RJ13013

Bartley, R., Roth, C. H., Ludwig, J., McJannet, D., Liedloff, A., Corfield, J., . . . Abbott, B. (2006). Runoff and erosion from Australia's tropical semi-arid rangelands: influence of ground cover for differing space and time scales. *Hydrological Processes, 20*(15), 3317-3333. doi:https://doi.org/10.1002/hyp.6334

Bartley, R., Thompson, C., Croke, J., Pietsch, T., Baker, B., Hughes, K., & Kinsey-Henderson, A. (2018). Insights into the history and timing of post-European land use disturbance on sedimentation rates in catchments draining to the Great Barrier Reef. *Marine Pollution Bulletin, 131*, 530-546. doi:https://doi.org/10.1016/j.marpolbul.2018.04.070

Bocco, G. (2016). Gully Erosion Analysis. Why Geopedology Matters? In A. J. Zinck, G. Metternicht, G. Bocco, & F. H. Del Valle (Eds.), *Geopedology: An Integration of Geomorphology and Pedology for Soil and Landscape Studies* (pp. 399-409). Cham: Springer International Publishing.

Bonell, M., & Williams, J. (1987). *Infiltration and redistribution of overland flow and sediment on a low relief landscape of semi-arid, tropical Queensland.* Paper presented at the Forest Hydrology and Watershed Management, Vancouver.

Borselli, L., Cassi, P., & Torri, D. (2008). Prolegomena to sediment and flow connectivity in the landscape: A GIS and field numerical assessment. *CATENA, 75*(3), 268-277. doi:http://dx.doi.org/10.1016/j.catena.2008.07.006

Bracken, L. J., & Croke, J. (2007). The concept of hydrological connectivity and its contribution to understanding runoff-dominated geomorphic systems. *Hydrological Processes, 21*, 1749-1763. doi:https://doi.org/10.1002/hyp.6313

Brasington, J., Langham, J., & Rumsby, B. (2003). Methodological sensitivity of morphometric estimates of coarse fluvial sediment transport. *Geomorphology, 53*(3), 299-316. doi:https://doi.org/10.1016/S0169-555X(02)00320-3

Brice, J. C. (1966). *Erosion and deposition in the loess-mantled Great Plains, Medicine Creek drainage basin, Nebraska.* (352H). Retrieved from http://pubs.er.usgs.gov/publication/pp352H

Brooks, A., Spencer, J., & Knight, J. (2009). Alluvial gully erosion: an example from the Mitchell fluvial megafan, Queensland, Australia. *Earth Surface Processes and Landforms, 34*, 43-48. doi:https://doi.org/10.1002/esp.1883

Bull, L., & Kirkby, M. (1997). Gully processes and modelling. *Progress in physical geography, 21*(3), 354-374. doi:https://doi.org/10.1177/030913339702100302

Caitcheon, G. G., Olley, J. M., Pantus, F., Hancock, G., & Leslie, C. (2012). The dominant erosion processes supplying fine sediment to three major rivers in tropical Australia, the Daly (NT), Mitchell (Qld) and Flinders (Qld) Rivers. *Geomorphology, 151–152*, 188-195. doi:http://dx.doi.org/10.1016/j.geomorph.2012.02.001

Callow, J. N., May, S. M., & Leopold, M. (2018). Drone photogrammetry and KMeans point cloud filtering to create high resolution topographic and inundation models of coastal sediment archives. *43*(12), 2603-2615. doi:https://doi.org/10.1002/esp.4419

Castillo, C., & Gómez, J. A. (2016). A century of gully erosion research: Urgency, complexity and study approaches. *Earth-Science Reviews, 160*, 300-319. doi:https://doi.org/10.1016/j.earscirev.2016.07.009

Castillo, C., Taguas, E. V., Zarco-Tejada, P., James, M. R., & Gómez, J. A. (2014). The normalized topographic method: an automated procedure for gully mapping using GIS. *Earth Surface Processes and Landforms, 39*(15), 2002-2015. doi: https://doi.org/10.1002/esp.3595

Cavalli, M. (2016). HydrogeomorphologyTools/ Connectivity-Index-ArcGIS-toolbox. Accessed 10 November 2018. Retrieved from https://github.com/HydrogeomorphologyTools10

Cavalli, M., Trevisani, S., Comiti, F., & Marchi, L. (2013). Geomorphometric assessment of spatial sediment connectivity in small Alpine catchments. *Geomorphology, 188*, 31-41. doi:https://doi.org/10.1016/j.geomorph.2012.05.007

Chartin, C., Evrard, O., Laceby, J. P., Onda, Y., Ottlé, C., Lefèvre, I., & Cerdan, O. (2017). The impact of typhoons on sediment connectivity: lessons learnt from contaminated coastal catchments of the Fukushima Prefecture (Japan). *42*(2), 306-317. doi:https://doi.org/10.1002/esp.4056

Chittleborough, D. J. (1992). Formation and pedology of duplex soils. *Australian Journal of Experimental Agriculture, 32*(7), 815-825. doi:http://dx.doi.org/10.1071/EA9920815

Coles, R. G., Rasheed, M. A., McKenzie, L. J., Grech, A., York, P. H., Sheaves, M., . . . Bryant, C. (2015). The Great Barrier Reef World Heritage Area seagrasses: Managing this iconic Australian ecosystem resource for the future. *Estuarine, Coastal and Shelf Science, 153*, A1-A12. doi:https://doi.org/10.1016/j.ecss.2014.07.020

Croke, J., Mockler, S., Fogarty, P., & Takken, I. (2005). Sediment concentration changes in runoff pathways from a forest road network and the resultant spatial pattern of catchment connectivity. *Geomorphology, 68*(3–4), 257-268. doi:http://dx.doi.org/10.1016/j.geomorph.2004.11.020

Daba, S., Rieger, W., & Strauss, P. (2003). Assessment of gully erosion in eastern Ethiopia using photogrammetric techniques. *CATENA, 50*(2–4), 273-291. doi:http://dx.doi.org/10.1016/S0341-8162(02)00135-2

De'ath, G., & Fabricius, K. (2010). Water quality as a regional driver of coral biodiversity and macroalgae on the Great Barrier Reef. *Ecological Applications, 20*(3), 840-850. doi:https://doi.org/10.1890/08-2023.1

DeLong, S. B., Youberg, A. M., DeLong, W. M., & Murphy, B. P. (2018). Post-wildfire landscape change and erosional processes from repeat terrestrial lidar in a steep headwater catchment, Chiricahua Mountains, Arizona, USA. *Geomorphology, 300*, 13-30. doi:https://doi.org/10.1016/j.geomorph.2017.09.028

Fox, G. A., Sheshukov, A., Cruse, R., Kolar, R. L., Guertault, L., Gesch, K. R., & Dutnell, R. C. (2016). Reservoir sedimentation and upstream sediment sources: perspectives and future research needs on streambank and gully erosion. *Environmental Management, 57*(5), 945-955. doi:https://doi.org/10.1007/s00267-016-0671-9

Fox, G. A., & Wilson, G. V. (2010). The role of subsurface flow in hillslope and stream bank erosion: a review. *Soil Science Society of America Journal, 74*(3), 717-733. doi:10.2136/sssaj2009.0319

Frankl, A., Stal, C., Abraha, A., Nyssen, J., Rieke-Zapp, D., De Wulf, A., & Poesen, J. (2015). Detailed recording of gully morphology in 3D through image-based modelling. *CATENA, 127*, 92-101. doi:http://dx.doi.org/10.1016/j.catena.2014.12.016

García-Ruiz, J. M. (2010). The effects of land uses on soil erosion in Spain: A review. *CATENA, 81*(1), 1-11. doi:http://dx.doi.org/10.1016/j.catena.2010.01.001

Gay, A., Cerdan, O., Mardhel, V., & Desmet, M. (2016). Application of an index of sediment connectivity in a lowland area. *Journal of Soils and Sediments, 16*(1), 280-293. doi:https://doi.org/10.1007/s11368-015-1235-y

Gilad, U., Denham, R., & Tindall, D. (2012). *Gullies, Google Earth and the Great Barrier Reef: A remote sensing methodology for mapping gullies over extensive areas.* Paper presented at the International Archives of the Photogrammetry, Remote Sensing and Spatial Information Science, Volume XXXIX-B8, Melbourne.

Girardeau-Montaut, D. (2018). CloudCompare: 3D point cloud and mesh processing software v2.9. v2.9. Accessed 10 November 2018. Retrieved from http://www.danielgm.net/cc/

Glendell, M., McShane, G., Farrow, L., James, M. R., Quinton, J., Anderson, K., . . . Brazier, R. E. (2017). Testing the utility of structure-from-motion photogrammetry reconstructions using small unmanned aerial vehicles and ground photography to estimate the extent of upland soil erosion. *Earth Surface Processes and Landforms, 42*(12), 1860-1871. doi:https://doi.org/10.1002/esp.4142

Heckmann, T., Cavalli, M., Cerdan, O., Foerster, S., Javaux, M., Lode, E., . . . Brardinoni, F. (2018). Indices of sediment connectivity: opportunities, challenges and limitations. *Earth-Science Reviews, 187*, 77-108. doi:https://doi.org/10.1016/j.earscirev.2018.08.004

Heckmann, T., & Vericat, D. (2018). Computing spatially distributed sediment delivery ratios: inferring functional sediment connectivity from repeat high-resolution digital elevation models. *43*(7), 1547-1554. doi:https://doi.org/10.1002/esp.4334

Horton, R. E. (1933). The role of infiltration in the hydrologic cycle. *Transactions American Geophysical Union, 14*(1), 446-460. doi:https://doi.org/10.1029/TR014i001p00446

Hughes, A. O., Olley, J. M., Croke, J. C., & McKergow, L. A. (2009). Sediment source changes over the last 250 years in a dry-tropical catchment, central Queensland, Australia. *Geomorphology, 104*(3–4), 262-275. doi:http://dx.doi.org/10.1016/j.geomorph.2008.09.003

Isbell, R. F. (1996). *The Australian soil classification* (revised first ed.). Collingwood: CSIRO Publishing.

James, M. R., & Robson, S. (2014). Mitigating systematic error in topographic models derived from UAV and ground-based image networks. *Earth Surface Processes and Landforms, 39*(10), 1413-1420. doi: https://doi.org/10.1002/esp.3609

James, M. R., Robson, S., d'Oleire-Oltmanns, S., & Niethammer, U. (2017). Optimising UAV topographic surveys processed with structure-from-motion: Ground control quality, quantity and bundle adjustment. *Geomorphology, 280*, 51-66. doi:http://dx.doi.org/10.1016/j.geomorph.2016.11.021

Jarihani, A. A., Callow, J. N., McVicar, T. R., Van Niel, T. G., & Larsen, J. R. (2015). Satellite-derived Digital Elevation Model (DEM) selection, preparation and correction for hydrodynamic modelling in large, low-gradient and data-sparse catchments. *Journal of hydrology, 524*, 489-506. doi:https://doi.org/10.1016/j.jhydrol.2015.02.049

Jarihani, B., Sidle, R., Bartley, R., Roth, C., & Wilkinson, S. (2017). Characterisation of Hydrological Response to Rainfall at Multi Spatio-Temporal Scales in Savannas of Semi-Arid Australia. *Water, 9*(7), 540. doi:https://doi.org/10.3390/w9070540

Javernick, L., Brasington, J., & Caruso, B. (2014). Modeling the topography of shallow braided rivers using Structure-from-Motion photogrammetry. *Geomorphology, 213*, 166-182. doi:http://dx.doi.org/10.1016/j.geomorph.2014.01.006

Jones, D. A., Wang, W., & Fawcett, R. (2009). High-quality spatial climate data-sets for Australia. *Australian Meteorological and Oceanographic Journal, 58*(4), 233. doi:10.22499/2.5804.003

Jungerius, P. D., Matundura, J., & van de Ancker, J. A. M. (2002). Road construction and gully erosion in West Pokot, Kenya. *Earth Surface Processes and Landforms, 27*(11), 1237-1247. doi:https://doi.org/10.1002/esp.423

Kaiser, A., Neugirg, F., Rock, G., Müller, C., Haas, F., Ries, J., & Schmidt, J. (2014). Small-Scale Surface Reconstruction and Volume Calculation of Soil Erosion in Complex Moroccan Gully Morphology Using Structure from Motion. *Remote Sensing, 6*(8), 7050-7080. doi:https://doi.org/10.3390/rs6087050

Kirkby, M. J., & Bracken, L. J. (2009). Gully processes and gully dynamics. *Earth Surface Processes and Landforms, 34*(14), 1841-1851. doi:https://doi.org/10.1002/esp.1866

Koci, J., Jarihani, B., Leon, J. X., Sidle, R., Wilkinson, S., & Bartley, R. (2017). Assessment of UAV and Ground-Based Structure from Motion with Multi-View Stereo Photogrammetry in a Gullied Savanna Catchment. *ISPRS International Journal of Geo-Information, 6*(11), 328. doi:https://doi.org/10.3390/ijgi6110328

Lane, S. N., Reaney, S. M., & Heathwaite, A. L. (2009). Representation of landscape hydrological connectivity using a topographically driven surface flow index. *Water Resources Research, 45*(8). doi: https://doi.org/10.1029/2008WR007336

Lewis, S. E., Shields, G. A., Kamber, B. S., & Lough, J. M. (2007). A multi-trace element coral record of land-use changes in the Burdekin River catchment, NE Australia. *Palaeogeography, Palaeoclimatology, Palaeoecology, 246*(2-4), 471-487. doi:https://doi.org/10.1016/j.palaeo.2006.10.021

Lindsay, J. B. (2016). Whitebox GAT: A case study in geomorphometric analysis. *Computers & Geosciences, 95*, 75-84. doi:https://doi.org/10.1016/j.cageo.2016.07.003

Liu, X. (2008). Airborne LiDAR for DEM generation: some critical issues. *Progress in physical geography, 32*(1), 31-49. doi:https://doi.org/10.1177/0309133308089496

Lizaga, I., Quijano, L., Palazón, L., Gaspar, L., & Navas, A. (2018). Enhancing Connectivity Index to Assess the Effects of Land Use Changes in a Mediterranean Catchment. *29*(3), 663-675. doi:https://doi.org/10.1002/ldr.2676

Ludwig, J. A., Wilcox, B. P., Breshears, D. D., Tongway, D. J., & Imeson, A. C. (2005). Vegetation patches and runoff-erosion as interacting ecohydrological processes in semiarid landscapes. *Ecology, 86*(2), 288-297. doi: https://doi.org/10.1890/03-0569

MacLeod, N. D., & McIvor, J. G. (2008). Quantifying production–environment tradeoffs for grazing land management — A case example from the Australian rangelands. *Ecological Economics, 65*(3), 488-497. doi:http://dx.doi.org/10.1016/j.ecolecon.2007.07.013

McCloskey, G., Waters, D., Baheerathan, R., Darr, S., Dougall, C., Ellis, R., Fentie, B., Hateley, L. (2017). *Modelling pollutant load changes due to improved management practices in the Great Barrier Reef catchments: updated methodology and results – Technical Report for Reef Report Card 2014.* Queensland Department of Natural Resources and Mines, Queensland Department of Natural Resources and Mines, Brisbane. Retrieved from https://www.reefplan.qld.gov.au/tracking-progress/reef-report-card

McIvor, J., Williams, J., & Gardener, C. (1995). Pasture management influences runoff and soil movement in the semi-arid tropics. *Australian Journal of Experimental Agriculture, 35*(1), 55-65. doi:http://dx.doi.org/10.1071/EA9950055

McKergow, L. A., Prosser, I. P., Hughes, A. O., & Brodie, J. (2005). Sources of sediment to the Great Barrier Reef World Heritage Area. *Marine Pollution Bulletin, 51*(1-4), 200-211. doi:https://doi.org/10.1016/j.marpolbul.2004.11.029

Mott, J. J., Williams, J., Andrew, M. H., & Gillison, A. N. (1985). Chapter 7: Australian savanna ecosystems. In J. C. Tothill & M. J.J (Eds.), *Ecology and management of the world's savannas* (pp. 56-82). Canberra: Australian Academy of Sciences.

Nicholls, N. (1991). The El Niño/ Southern Oscillation and Australian Vegetation. *Vegetatio, 91*(1/2), 23-36. doi:http://www.jstor.org/stable/20038710

Nyssen, J., Poesen, J., Moeyersons, J., Luyten, E., Veyret-Picot, M., Deckers, J., . . . Govers, G. (2002). Impact of road building on gully erosion risk: a case study from the Northern Ethiopian Highlands. *Earth Surface Processes and Landforms, 27*(12), 1267-1283. doi: https://doi.org/10.1002/esp.404

Olley, J., Brooks, A., Spencer, J., Pietsch, T., & Borombovits, D. (2013). Subsoil erosion dominates the supply of fine sediment to rivers draining into Princess Charlotte Bay, Australia. *Journal of Environmental Radioactivity, 124*, 121-129. doi:http://dx.doi.org/10.1016/j.jenvrad.2013.04.010

Patton, P. C., & Schumm, S. A. (1975). Gully erosion, Northwestern Colarado: a threshold phenomenon. *Geology, 3*(2), 88-90. doi:https://doi.org/10.1130/0091-7613(1975)3<88:GENCAT>2.0.CO;2

Poesen, J. (2018). Soil erosion in the Anthropocene: Research needs. *Earth Surface Processes and Landforms, 43*(1), 64-84. doi:https://doi.org/10.1002/esp.4250

Poesen, J., Nachtergaele, J., Verstraeten, G., & Valentin, C. (2003). Gully erosion and environmental change: importance and research needs. *CATENA, 50*(2–4), 91-133. doi:http://dx.doi.org/10.1016/S0341-8162(02)00143-1

Prosser, I. P., & Winchester, S. J. (1996). History and processes of gully initiation and development in eastern Australia. *Zeitschrift fur Geomorphologie, Suppl. Bund, 105*, 91-109.

Queensland, S. o. (2012). Gully Presence Map 5km 2012 Burdekin Catchment. (P66G Gully mapping and drivers in grazing lands). Retrieved 3 February 2018, from Department of Environment and Science, Queensland Spatial Catalogue http://qldspatial.information.qld.gov.au/catalogue/custom/detail.page?fid={1D47A676-8092-4147-A9CD-51833C3CCE05}

Riverscapes Consortium. (2018). Geomorphic Change Detection Software. Accessed 10 November 2018. Retrieved from http://gcd.riverscapes.xyz/Download/

Roth, C. H. (2004). A framework relating soil surface condition to infiltration and sediment and nutrient mobilization in grazed rangelands of northeastern Queensland, Australia. *Earth Surface Processes and Landforms, 29*(9), 1093-1104. doi:https://doi.org/10.1002/esp.1104

Ryan, J., McAlpine, C., Ludwig, J., & Callow, J. (2015). Modelling the Potential of Integrated Vegetation Bands (IVB) to Retain Stormwater Runoff on Steep Hillslopes of Southeast Queensland, Australia. *Land, 4*(3), 711. doi:https://doi.org/10.3390/land4030711

Shellberg, J., Brooks, A., & Spencer, J. (2010). *Land-use change from indigenous management to cattle grazing initiates the gullying of alluvial soils in northern Australia*. Paper presented at the Proceedings of the 19th World Congress of Soil Science: Soil solutions for a changing world, Brisbane.

Shellberg, J. G., Brooks, A. P., Spencer, J., & Ward, D. (2013). The hydrogeomorphic influences on alluvial gully erosion along the Mitchell River fluvial megafan. *Hydrological Processes, 27*(7), 1086-1104. doi:https://doi.org/10.1002/hyp.9240

Shellberg, J. G., Spencer, J., Brooks, A. P., & Pietsch, T. J. (2016). Degradation of the Mitchell River fluvial megafan by alluvial gully erosion increased by post-European land use change, Queensland, Australia. *Geomorphology, 266*, 105-120. doi:http://dx.doi.org/10.1016/j.geomorph.2016.04.021

Sidle, R. C., Gomi, T., Loaiza Usuga, J. C., & Jarihani, B. (2017). Hydrogeomorphic processes and scaling issues in the continuum from soil pedons to catchments. *Earth-Science Reviews, 175*, 75-96. doi:https://doi.org/10.1016/j.earscirev.2017.10.010

Sidle, R. C., Jarihani, B., Kaka, S. I., Koci, J., & Al-Shaibani, A. (2019). Hydrogeomorphic processes affecting dryland gully erosion: Implications for modelling. *Progress in Physical Geography: Earth and Environment, 43*(1), 46-64. doi:https://doi.org/10.1177/0309133318819403

Sidle, R. C., Sasaki, S., Otsuki, M., Noguchi, S., & Rahim Nik, A. (2004). Sediment pathways in a tropical forest: effects of logging roads and skid trails. *Hydrological Processes, 18*(4), 703-720. doi: https://doi.org/10.1002/hyp.1364

Sidle, R. C., & Ziegler, A. D. (2010). Elephant Trail Runoff and Sediment Dynamics in Northern Thailand. *Journal of Environmental Quality, 39*(3), 871-881. doi:10.2134/jeq2009.0218

Sidle, R. C., Ziegler, A. D., Negishi, J. N., Nik, A. R., Siew, R., & Turkelboom, F. (2006). Erosion processes in steep terrain—Truths, myths, and uncertainties related to forest management in Southeast Asia. *Forest Ecology and Management, 224*(1–2), 199-225. doi:http://dx.doi.org/10.1016/j.foreco.2005.12.019

Smith, M. W., Carrivick, J. L., & Quincey, D. J. (2015). Structure from motion photogrammetry in physical geography. *Progress in physical geography*, 1-29. doi:https://doi.org/10.1177/0309133315615805

Smith, M. W., & Vericat, D. (2015). From experimental plots to experimental landscapes: topography, erosion and deposition in sub‐humid badlands from Structure‐from‐Motion photogrammetry. *Earth Surface Processes and Landforms, 40*(12), 1656-1671. doi: https://doi.org/10.1002/esp.3747

State of Queensland. (2018). *Reef 2050 Water Quality Improvement Plan: 2017-2022.* Reef Water Quality Protection Plan Secretariat, Brisbane. Retrieved from https://www.reefplan.qld.gov.au/about/

Thomas, M. F. (1994). *Geomorphology in the tropics: a study of weathering and denudation in low latitudes*. West Sussex: John Wiley & Sons.

Tindall, D., Marchand, B., Gilad, U., Goodwin, N., Denham, R., & Byer, S. (2014). *Gully mapping and drivers in the grazing lands of the Burdekin catchment. RP66G Synthesis Report.* State of Queensland (Department of Science, Information Technology, Innovation and the Arts), Brisbane. Retrieved from https://publications.qld.gov.au/dataset/gully-mapping-burdekin

Torri, D., & Poesen, J. (2014). A review of topographic threshold conditions for gully head development in different environments. *Earth-Science Reviews, 130*(0), 73-85. doi:http://dx.doi.org/10.1016/j.earscirev.2013.12.006

Vanmaercke, M., Poesen, J., Van Mele, B., Demuzere, M., Bruynseels, A., Golosov, V., . . . Yermolaev, O. (2016). How fast do gully headcuts retreat? *Earth-Science Reviews, 154*, 336-355. doi:http://dx.doi.org/10.1016/j.earscirev.2016.01.009

Wantzen, K. M. (2006). Physical pollution: effects of gully erosion on benthic invertebrates in a tropical clear-water stream. *Aquatic Conservation: Marine and Freshwater Ecosystems, 16*(7), 733-749. doi:https://doi.org/10.1002/aqc.813

Waterhouse, J., Schaffelke, B., Bartley, R., Eberhard, R., Brodie, J., Star, M., . . . Kroon, F. (2017). *2017 Scientific Consensus Statement: Land use impacts on Great Barrier Reef water quality and ecosystem condition.* The State of Queensland, Brisbane. Retrieved from https://www.reefplan.qld.gov.au/about/reef-science/scientific-consensus-statement/

Westoby, M. J., Brasington, J., Glasser, N. F., Hambrey, M. J., & Reynolds, J. M. (2012). 'Structure-from-Motion' photogrammetry: A low-cost, effective tool for geoscience applications. *Geomorphology, 179*, 300-314. doi:http://dx.doi.org/10.1016/j.geomorph.2012.08.021

Wheaton, J. M., Brasington, J., Darby, S. E., & Sear, D. A. (2010). Accounting for uncertainty in DEMs from repeat topographic surveys: improved sediment budgets. *Earth Surface Processes and Landforms, 35*(2), 136-156. doi:https://doi.org/10.1002/esp.1886

Wilkinson, S. N., Bartley, R., Hairsine, P. B., Bui E.N, Gregory L, & A.E, H. (2015). *Managing gully erosion as an efficient approach to improving water quality in the Great Barrier Reef lagoon. Report to the Department of the Environment.* CSIRO Land and Water, Canberra. Retrieved from https://publications.csiro.au/rpr/download?pid=csiro:EP1410201&dsid=DS6

Wilkinson, S. N., Hancock, G. J., Bartley, R., Hawdon, A. A., & Keen, R. (2013). Using sediment tracing to assess processes and spatial patterns of erosion in grazed rangelands, Burdekin River basin, Queensland, Australia. *Agriculture, Ecosystems and Environment, 180*, 90-102. doi:https://doi.org/10.1016/j.agee.2012.02.002

Wilkinson, S. N., Kinsey‐Henderson, A. E., Hawdon, A. A., Hairsine, P. B., Bartley, R., & Baker, B. (2018). Grazing impacts on gully dynamics indicate approaches for gully erosion control in northeast Australia. *Earth Surface Processes and Landforms, 43*, 1711–1725. doi:https://doi.org/10.1002/esp.4339

Tables

Table 1. Survey parameters used in the 2018 Unmanned Aircraft System (UAS) and Ground-based (GB) survey. Note, the same UAS survey parameters were applied in 2017 and 2018, with the exception that in 2017, camera focus was set to automatic. For the GB survey, the same survey parameters were applied across all survey years, with the exception that only 10 Ground Control Points (GCP) were used in 2016. In 2016 and 2017, an Ashtech Magellan Promark 500 Real Time Kinematic Global Navigation Satellite System (RTK GNSS receiver) was used to survey GCPs and validation points (10 mm horizontal and 20 mm vertical manufacturer accuracy).

Parameter	UAS Survey	GB Survey
Platform	DJI Phantom 4 Advanced	Panasonic GH3
Lens	DJI 8.8 mm (35 mm equivalent = 24 mm)	Panasonic Lumix G 20 mm (35 mm equivalent = 40 mm), Mark II, ASPH
Sensor	1” CMOS	4/3″ CMOS
Sensor resolution	20 MP	16 MP
Image resolution	20 MP	8 MP
ISO	Auto	Auto
Aperture	Auto	Auto
Shutter speed	1/800	Auto
Focus	∞	Auto
Mission planning	DJI Ground Station Pro	NA
Image capture height (m AGL)	60 m	~ 1.5 m
Ground sampling distance	~1.6 cm pixel^{-1}	~ 0.1 cm pixel^{-1}
Image capture pattern	Double grid	See Koci *et al.* (2017)
Viewing angle	Nadir, Off-Nadir (30°)	Typically between 10 – 30°
Overlap	Nadir: 90% Forward, 75% Side Off-Nadir: 40% Forward, 40% Side	Typically > 9 images for a given area, captured from various perspectives
Survey area	~150,000 m^2	~ 300 – 700 m^2
Number of photos	~ 1500 - 2000	~ 1000 - 1500
Number of GCPs	20	32
RTK GNSS receiver model (manufacturer horizontal and vertical accuracy, mm)	CHC i80 (8, 15)	CHC i80 (8, 15)

Table 2. Agisoft PhotoScan processing parameters and workflow. UAS: Unmanned Aircraft System; GB: Ground-based; RTK GNSS: Real Time Kinematic Global Navigation Satellite System; GCP: Ground Control Point.

Step	**Description**
1. Image alignment and sparse point cloud clean	• Align images using 'high' accuracy setting. • Clean sparse point cloud using gradual selection tool: - Reconstruction uncertainty: Level = ~10 and ~50 for UAS and GB surveys, respectively. - Projection accuracy: Level = ~3 for both UAS and GB survey.
2. Scaling and Georeferencing	• Import coordinates of GCPs and identify their precise location. • Adjust reference settings to be 'physically realistic' (James et al., 2017): - Marker accuracy (m) = 0.02 m, reflecting RTK GNSS survey accuracy. - Marker accuracy (pixel) = 0.5 pix, reflecting approximate root mean square error of GCPs. - Tie point accuracy (pixel) = 0.3 pix, reflecting approximate root mean square reprojection error of tie points.
3. Sparse point cloud clean and model optimisation	• Clean sparse point cloud using gradual selection tool: - Reprojection error: Level = ~3 for both UAS and GB survey. • Optimise sparse point cloud: - Use the sfm_georef tool (James et al., 2017) to determine optimal camera model parameter set[†].
4. Dense point cloud generation and classification	• Build dense point cloud. • Classify 'ground' and 'non-ground' points using 'Classify': - Cell size: 5 m; - Maximum distance: 0.25 m; - Maximum angle: 15°.
5. Ortho-photo mosaic generation	• Build mesh. • Build texture. • Build ortho-photo mosaic.

[†] *In this study, investigation of the effect of different camera model parameters sets on overall network performance using the sfm_georef V3.1 tool (James et al., 2017), revealed negligible (mm-scale) variations in the root mean square error (RMSE) of control and check points, for both UAS and GB surveys. The default camera model, including f, c1, c2, k1, k2, k3, p1 and p2 parameters, aligning to model C of James* et al. *(2017) and Callow* et al. *(2018), was used in the optimisation procedure.*

Table 3. Root mean square elevation error (m) in the comparison of independant RTK GNSS validation points (i.e., points not used in SfM georeferencing) and points extracted from Unmanned Aircraft System (UAS) and Ground-based DEMs (U- and G-DEM, respectively). n: number of validation points; RMSE: root mean square error; NA: not applicable.

Gully system	**Survey area**	**U-DEM**				**G-DEM**					
		2017		**2018**		**2016**		**2017**		**2018**	
		n	**RMSE**	***n***	**RMSE**	***n***	**RMSE**	***n***	**RMSE**	***n***	**RMSE**
G1	**Gully**	262	0.13	263	0.05	159	0.06	262	0.07	263	0.06
	Hillslope	682	0.10	460	0.07	NA	NA	NA	NA	NA	NA
G3	**Gully**	120	0.13	232	0.12	158	0.07	120	0.08	232	0.07
	Hillslope	488	0.12	539	0.09	NA	NA	NA	NA	NA	NA
G6	**Gully**	136	0.13	194	0.06	222	0.06	136	0.04	194	0.03
	Hillslope	521	0.10	408	0.06	NA	NA	NA	NA	NA	NA
G8	**Gully**	171	0.06	276	0.10	168	0.04	171	0.03	276	0.03
	Hillslope	591	0.07	439	0.09	NA	NA	NA	NA	NA	NA

Table 4. Gully volumetric change over the two-year study period (2016-2018), derived from Ground-based (GB) DEMs of Difference (minimum level of detection = 0.2 m). Negative values indicate net erosion.

Site	**Net volume change (m^3)**		
	2016 – 2017	**2017 – 2018**	**2016 – 2018**
G1	-1.2	-9.1	-17.1
G3	-0.2	-2.7	-3.0
G6	0.2	-2.4	-3.1
G8	-4.0	-8.1	-18.5

Table 5. Area, mean slope, and Index of Connectivity (IC) statistics for the catchment areas of headcuts, derived from the 2017 UAS survey, and linear, areal and volumetric headcut retreat, derived from Unmanned Aircraft System (UAS) DEMs of Difference (minimum level of detection = 0.3 m) between 2017 and 2018. Min: minimum; Max: maximum, Std. Dev.: standard deviation.

Headcut	**Area (m^2)**	**Mean slope ($m\ m^{-1}$)**	**Mean IC**	**Min. IC**	**Max. IC**	**Std. Dev. IC**	**Linear headcut retreat ($m\ yr^{-1}$)**	**Areal headcut retreat ($m^2\ yr^{-1}$)**	**Volume headcut retreat ($m^3\ yr^{-1}$)**
G1									
G1HC1	6939.9	0.071	-5.207	-7.278	-0.542	0.643	0.3	0.93	0.660
G1HC2	2313.9	0.072	-5.050	-7.026	0.825	0.630	0.2	1.36	0.861
G1HC3	4714.4	0.069	-5.002	-7.263	0.821	0.607	0.2	0.66	0.378
G3									
G3HC1	48363.8	0.147	-5.435	-7.568	0.105	0.462	0.1	1.22	0.658
G3HC2	13489.2	0.158	-5.140	-7.253	-0.044	0.494	0.2	1.70	0.793
G3HC3	966.0	0.140	-4.697	-6.463	-0.827	0.470	0.2	0.27	0.010
G3HC4	5074.2	0.145	-5.062	-7.199	0.959	0.544	0.0	0.0	0.0
G6									
G6HC1	6169.1	0.158	-5.031	-7.126	1.005	0.601	0.1	0.45	0.174
G6HC2	343.7	0.120	-4.191	-6.405	-0.595	0.692	0.1	0.15	0.050
G6HC3	6675.3	0.144	-5.140	-7.139	-0.517	0.585	0.1	0.19	0.068
G6HC4	6897.5	0.149	-4.941	-6.948	-0.351	0.597	0.2	0.79	0.325
G6HC5	8402.2	0.141	-5.123	-7.499	-0.295	0.702	0.1	2.22	1.229
G6HC6	87.3	0.173	-3.332	-5.129	-0.287	0.651	0.2	0.01	0.003
G6HC7	106.2	0.150	-3.585	-5.596	-0.112	0.699	0.2	0.18	0.064
G6HC8	440.1	0.150	-3.874	-5.914	-0.214	0.755	0.1	0.63	0.241
G8									
G8HC1	6638.3	0.080	-5.508	-7.232	-0.053	0.670	0.3	8.99	4.188
G8HC2	1570.4	0.071	-5.008	-6.672	-0.062	0.719	0.3	3.43	1.557
G8HC3	904.9	0.070	-4.831	-6.672	-0.159	0.782	0.2	1.73	0.830
G8HC4	697.5	0.077	-4.494	-6.447	-0.054	0.833	0.1	0.23	0.078
G8HC5	6287.8	0.067	-5.107	-6.961	-1.009	0.611	0.2	2.52	1.651
G8HC6	4582.8	0.080	-5.182	-6.757	-0.528	0.555	0.1	0.94	0.322

Figure legends

Figure 1. Map showing the location of the study sites within the Weany Creek and Wheel Creek catchments, within the Upper Burdekin catchment and part of the Burdekin River Basin. The gully probability mapping is available from the State of Queensland (2012). The hillshaded Digital Elevation Models (DEMs) are derived from airborne Light Detection and Ranging (LiDAR) captured in 2013, outlined in Tindall *et al.* (2014).

Figure 2. Ground-based Digital Surface Models of: (a) G1; (b) G3; (c) G6; and (d) G8, with inset photographs used in the Structure-from-Motion photogrammetry procedure.

Figure 3. Histogram showing the distribution of difference in elevation between independently surveyed Real Time Kinematic Global Navigation Satellite System (RTK GNSS) validation points (i.e. point not used in Structure-From-Motion georeferencing) and concordant points extracted from (a) Unmanned Aircraft System DEM (U-DEM); and (b) Ground-based DEM (G-DEM), for the 2018 survey of G3. Map showing the magnitude of difference in elevation between RTK GNSS validation points and concordant points extracted from the (c) U-DEM; and (d) G-DEM, for the 2018 survey of G3. Comparison of cross-sectional profiles among different survey platforms across (e) G3; and (f) G8, for the 2018 survey.

Figure 4. Major hydrological flow lines (contributing area > 100 m^2) (left panel), and minor hydrological flow lines (contributing area > 10 m^2) and gully geomorphic change (0.2 m minimum level of detection) between 2016 and 2018 (right panel) at: (a) G1; (b) G3; (c) G6; and (d) G8.

Figure 5. Index of connectivity (IC) calculated with respect to the main channel at: (a) G1; (b) G3; (c) G6; and (d) G8. The catchment areas of the major headcuts within each gully system are also shown. High IC pathways were classified with four bins defined and high IC values considered to be within the range of lower 3 bins. Inset graphics are Ground-based Structure-from-Motion with Multi-View Stereo photogrammetry reconstructions at the gully head with arrows indicating likely path of headcut retreat.

Figure 6. Hydrological flow pathways (contributing area > 100m^2) in contributing area of G8 Headcut 1. Black arrows indicate where cattle trails capture and re-orientate overland flow. Solid circle around arrow indicates where a break of slope on an unpaved road becomes a major hydrological flow pathway. Dashed circle indicates a scalded (i.e., persistently bare) area adjacent to an actively eroding gully.

Figure 7. Relationship between volumetric headcut retreat (derived from Unmanned Aircraft System DEMs of Difference analysis between 2017 and 2018 survey) and: (a) headcut catchment area; (b) headcut mean catchment slope; and (c) headcut mean IC value.

SUPPLEMENTARY MATERIALS

Supplementary material 1

Table S1. Summary of rainfall recorded near to the monitored gully systems (see Figure 1). The water years of 2015/2016, 2016/2017, and 2017/2018, are denoted as '15/16', '16/17' and '17/18', respectively. A water year commences on July 1 and ceases June 30. NA: Not Available; SP: Study Period. Negative values indicate the study period annual rainfall was lower than the long-term mean annual rainfall. Long-term (1900-2012) mean annual rainfall estimated using the AWAP gridded monthly rainfall dataset for Australia (Jones *et al.*, 2009).

		G1			**G3**			**G6**			**G8**	
	15/16	**16/17**	**17/18**	**15/16**	**16/17**	**17/18**	**15/16**	**16/17**	**17/18**	**15/16**	**16/17**	**17/18**
SP annual rainfall	581.4	744.8	835.8	630.0	688.0	774.4	568.4	667	665.8	NA	652	838
Difference between SP annual rainfall and long-term mean annual rainfall (%)	-15.2	8.6	21.8	-8.2	0.3	12.9	-17.1	-2.8	-2.9	NA	-16.6	7.2
Number of days with > 50 mm	4	5	4	4	4	3	3	3	2	NA	3	3
Peak daily intensity (mm day^{-1})	139.8	111.8	135.6	139.4	106.4	117.4	87.2	108	111	NA	102.2	148.8
Peak hourly intensity (mm hour^{-1})	98.0	39.6	45.0	109.0	45.2	17.4	76	37.8	30.8	NA	24	57.4
Peak 30 min. intensity (mm 30 min^{-1})	80.6	32.8	33.8	109.0	NA	17.4	63.6	32.2	NA	NA	NA	32

Supplementary material 2

Figure S1. (a) Boxplots of saturated hydraulic conductivity (Ksat) on trails, scalds and litter/vegetated land types. x = mean concentration, within box centre horizontal line = median concentration, within box upper and lower horizontal lines = upper and lower quartiles respectively, vertical black lines denote 1.5 times the interquartile range, circles indicate outlier points. Ksat was measured with a Mini Disk Infiltrometer at 15 sites for each land type. Photograph of infiltration measurement at (a) trail; (b) scald; and (c) litter land types.

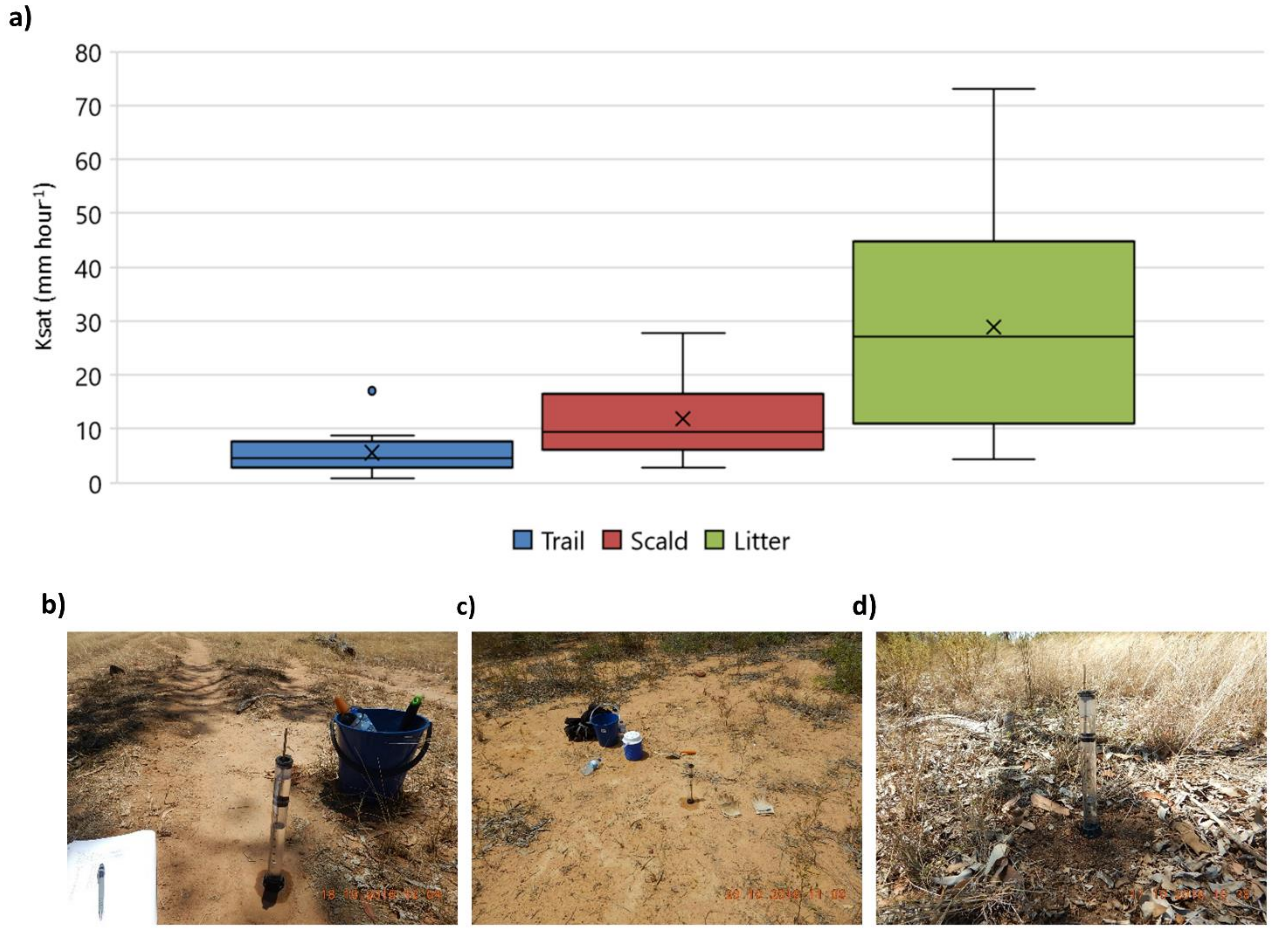

Supplementary material 3.

Table S2. Georeferencing error of Ground Control Points (GCPs) for the Unmanned Aircraft System (UAS) and Ground-based (GB) survey. Error (m) is calculated as the root mean square error between the actual position of the GCPs, derived from Real Time Kinematic Global Navigation Satellite System (RTK GNSS) measurements, and the estimated position of the GCPs, derived from the Structure-from-Motion photogrammetry model. Error (pixel, 'pix.') is calculated as the root mean square reprojection error for the GCPs calculated over all photos where the GCPs are visible. Years 2016, 2017, and 2018, are denoted as 16', 17' and 18', respectively. X: x-coordinate; Y: y-coordinate; Z: elevation coordinate.

Error	**G1**					**G3**					**G6**					**G8**				
	UAS		**Ground**			**UAS**		**Ground**			**UAS**		**Ground**			**UAS**		**Ground**		
	17'	**18'**	**16'**	**17'**	**18'**	**17'**	**18'**	**16'**	**17'**	**18'**	**17'**	**18'**	**16'**	**17'**	**18'**	**17'**	**18'**	**16'**	**17'**	**18'**
X (m)	0.032	0.026	0.014	0.021	0.008	0.018	0.028	0.007	0.002	0.010	0.031	0.031	0.006	0.029	0.011	0.023	0.043	0.009	0.011	0.011
Y (m)	0.039	0.028	0.009	0.024	0.009	0.023	0.023	0.009	0.002	0.008	0.023	0.021	0.011	0.022	0.008	0.021	0.037	0.008	0.013	0.010
Z (m)	0.061	0.033	0.026	0.013	0.013	0.026	0.036	0.012	0.002	0.013	0.070	0.052	0.010	0.021	0.015	0.079	0.048	0.005	0.012	0.008
Total (m)	0.079	0.050	0.031	0.035	0.018	0.039	0.051	0.017	0.004	0.018	0.082	0.064	0.016	0.038	0.020	0.085	0.073	0.013	0.020	0.017
Total (pix.)	0.445	0.482	0.661	0.639	0.570	0.591	0.511	0.682	0.574	0.497	0.707	0.568	1.029	0.572	0.569	0.573	0.486	0.810	0.613	0.648